THE ROLE OF ACTIVE REGION LOOP GEOMETRY. I. HOW CAN IT AFFECT CORONAL SEISMOLOGY?

M. SELWA[1,2,5], L. OFMAN[1,2,,6], AND S. K. SOLANKI[3,4]

[1] Department of Physics, The Catholic University of America, 620 Michigan Avenue, NE, 200 Hannan Hall, Washington, DC 20064, USA;
mselwa@mcs.st-and.ac.uk, leon.ofman@nasa.gov
[2] NASA Goddard Space Flight Center, Code 671, Greenbelt, MD 20771, USA
[3] Max-Planck-Institut für Sonnensystemforschung, Max-Planck-Str. 2, 37191 Katlenburg-Lindau, Germany; solanki@mps.mpg.de
[4] School of Space Research, Kyung Hee University, Yongin, Gyeonggi 446-701, Korea

ABSTRACT

We present numerical results of coronal loop oscillation excitation using a three-dimensional (3D) MHD model of an idealized active region (AR) field. The AR is initialized as a potential dipole magnetic configuration with gravitationally stratified density and contains a loop with a higher density than its surroundings. We study different ways of excitation of vertical kink oscillations of this loop by velocity: as an initial condition, and as an impulsive excitation with a pulse of a given position, duration, and amplitude. We vary the geometry of the loop in the 3D MHD model and find that it affects both the period of oscillations and the synthetic observations (difference images) that we get from oscillations. Due to the overestimated effective length of the loop in the case of loops which have maximum separation between their legs above the footpoints (>50% of observed loops), the magnetic field obtained from coronal seismology can also be overestimated. The 3D MHD model shows how the accuracy of magnetic field strength determined from coronal seismology can be improved. We study the damping mechanism of the oscillations and find that vertical kink waves in 3D stratified geometry are damped mainly due to wave leakage in the horizontal direction.

Key words: magnetohydrodynamics (MHD) – Sun: corona – Sun: oscillations

Online-only material: color figures

1. INTRODUCTION

Solar space based Extreme Ultraviolet (EUV) telescopes such as SUMER on board the *Solar and Heliospheric Observatory* and the *Transition Region and Coronal Explorer* (*TRACE*) facilitated in the detection of various oscillation modes in solar coronal loops. The most important discoveries concern propagating (Berghmans & Clette 1999; Robbrecht et al. 1999; De Moortel et al. 2002) and standing (Kliem et al. 2002; Wang et al. 2002) slow magnetosonic waves as well as observations of fast kink magnetosonic waves (Nakariakov et al. 1999; Aschwanden et al. 1999; Aschwanden et al. 2002; Schrijver et al. 2002; Wang & Solanki 2004). Kliem et al. (2002) discovered periodic Doppler shift oscillations associated with flares and interpreted them as MHD waves. The oscillations were later identified as standing slow magnetosonic waves by Wang et al. (2003). The third branch of detected waves consists of short period fast sausage waves (Nakariakov et al. 2003; Aschwanden et al. 2004).

Among fast kink waves two kinds of oscillations may be distinguished: horizontal (Nakariakov et al. 1999; Aschwanden et al. 1999; Aschwanden et al. 2002; Schrijver et al. 2002) and vertical (Wang & Solanki 2004). Both of them lead to an asymmetric displacement of the loop, with the difference, however, that vertical oscillations are planar oscillations while horizontal oscillations are fully three-dimensional (3D) oscillations. They also differ in how they affect loop properties: vertical oscillations can change the loop length and as such are compressible, while the loop length remains fixed for horizontal oscillations.

Other properties, such as period and damping time do not vary significantly between these types or polarizations of kink mode oscillations.

One common feature of these observations is that the oscillations decay quite rapidly. Several mechanisms have been suggested to explain the rapid damping of loop oscillations, e.g., wave leakage (Smith et al. 1997; Selwa et al. 2007), enhanced viscosity (Nakariakov et al. 1999), resonant absorption (Ruderman & Roberts 2002), and phase mixing (Ofman & Aschwanden 2002). Ofman & Wang (2002) showed that thermal conduction can account for the damping of slow mode waves observed by SUMER. Resonant absorption was studied in 3D geometry (Ruderman & Roberts 2002), but the authors restricted their study to the linear regime and a straight cylindrical loop. Nonlinear 3D MHD studies of loop oscillation damping by wave leakage in curved (dipolar) active region (AR) geometry were performed recently by McLaughlin & Ofman (2008) and Selwa & Ofman (2009, 2010); see also the review by Ofman (2009b). They found that fieldline curvature can significantly enhance the leakage rate compared to a straight cylindrical loop with the same parameters.

Kink oscillations in coronal loops (usually represented by straight cylinders or slabs) have been studied for decades. Properties of waves in 3D straight loops were described by Roberts et al. (1984). The authors suggested that magnetoacoustic oscillations provide a potentially useful diagnostic tool for determining physical conditions in the inhomogeneous corona. Reviews of different oscillation properties including other effects such as stratification, expansion, twist, non-circular cross section, curvature, and collective behavior have been given by Nakariakov & Verwichte (2005) and Ruderman & Erdélyi (2009). More properties of oscillations in curved structures are provided by van Doorsselaere et al. (2009). The authors show that

---

[5] Present address: School of Mathematics and Statistics, University of St. Andrews, North Haugh, St. Andrews, Fife, KY16 9SS, UK.
[6] Visiting Associate Professor, Department of Geophysics and Planetary Sciences, Tel Aviv University, Ramat Aviv, Tel Aviv, Israel.

curvature introduces leakage effect. Recently, different methods of excitation of kink waves were studied. The most common way is an initial perturbation (Selwa et al. 2005, 2006, 2007) or a time-dependent pulse (Ofman 2007; Selwa & Ofman 2009). Selwa & Ofman (2010) compared the external excitation mechanism with an internal excitation mechanism and found that in complex ARs only the external one could reproduce observed time signatures of loop oscillations. Another type of excitation studied recently is the periodic shedding of Alfvénic vortices which can explain the excitation of some of the horizontally polarized kink oscillations (Nakariakov et al. 2009; Gruszecki et al. 2010).

Full 3D simulations of simultaneously excited vertical and horizontal oscillations were performed by McLaughlin & Ofman (2008). However, this model neglects several issues. The main simplification is that the loop density enhancement does not expand with the flux tube height. Recently, Pascoe et al. (2009) studied impulsively excited oscillations in an arcade loop. The authors found that the global transverse kink mode is efficiently excited for a range of attack angles (angles measured at the height of the apex of the loop from the line perpendicular to the loop in the horizontal direction) for pulses located at the height of the loop's apex. However, the amplitude of the oscillations decreases with the angle, while the frequency remains the same. Selwa & Ofman (2010) showed that observed kink oscillations are likely to be excited by external drivers only, and the curved topology of AR loops is necessary to understand the whole dynamics of loop oscillations. Selwa & Ofman (2009) studied transverse oscillations in a 3D curved gravity-free loop and slow standing mode in a curved dipolar stratified loop. Other 3D numerical simulations concern straight cylindrical loops. Propagating waves (slow, fast kink, and sausage) were studied by Selwa et al. (2004). Terradas & Ofman (2004) used 1D, 2D, and 3D models to explain density enhancements within the loop. Ofman (2005) studied kink waves and presented several 3D models of the loops including straight cylinder and four cylindrical loops. Ofman (2009a) studied the behavior of multiple cylindrical twisted loops. Ofman & Thompson (2002) and Ofman (2007) studied wave behavior in 3D ARs based on a dipole field and magnetogram data, respectively. However, their models did not include a denser loop structure, which is necessary to examine wave trapping and leakage.

In this paper, we focus mainly on simulations of fast kink oscillations. One goal of this paper is to extend the Ofman & Thompson (2002), McLaughlin & Ofman (2008), and Selwa & Ofman (2009, 2010) models. Ofman & Thompson (2002) studied the waves in an AR modeled as a dipole magnetic field with a gravitationally stratified atmosphere. McLaughlin & Ofman (2008) extended that model by adding a curved denser cylindrical loop that follows a chosen fieldline in the AR. However, their loop had a constant circular cross section which is an unrealistic model of a loop in a potential dipole field. Selwa & Ofman (2009, 2010) extended the model by adding a denser loop with variable cross section that expands with height in accordance with the flux tube structure in the dipole field. We vary the properties (mainly geometrical) of the pulse and the loop in order to better understand the mechanisms of excitation and damping of kink oscillations and their effect on coronal seismology.

The paper is organized as follows. The numerical model is described in Section 2. The numerical results are presented in Section 3. The paper is concluded by a short summary of the main results in Section 4.

2. NUMERICAL MODEL

We describe solar plasma with the 3D nonlinear dimensionless resistive MHD equations with gravitational effects included:

$$\frac{\partial \varrho}{\partial t} + \nabla \cdot (\varrho \mathbf{V}) = 0 \,, \tag{1}$$

$$\varrho \left[\frac{\partial \mathbf{V}}{\partial t} + (\mathbf{V} \cdot \nabla) \mathbf{V} \right] = -E_u \nabla p + (\nabla \times \mathbf{B}) \times \mathbf{B}$$
$$- \frac{\varrho \hat{\mathbf{z}}}{F_r (R_s + z - z_{\min})^2} \,, \tag{2}$$

$$\frac{\partial \mathbf{B}}{\partial t} = \nabla \times (\mathbf{V} \times \mathbf{B}) + \frac{1}{S} \nabla^2 \mathbf{B} \,. \tag{3}$$

Here ϱ denotes the mass density, $\mathbf{V}$ is the plasma velocity, $\mathbf{B}$ is the divergence-free ($\nabla \cdot \mathbf{B} = 0$) magnetic field vector, p is plasma pressure, R_s is solar radius, and $\hat{\mathbf{z}}$ is the unit vector in the vertical direction. The approximate form of the gravity term is applicable for the Cartesian box in our study. The dimensionless Euler number E_u, Froude number F_r, and Lundquist number S, are given as

$$E_u = \frac{\beta}{2} = \frac{c_s^2}{\gamma c_A^2}, \tag{4}$$

$$F_r = \frac{V_0^2 L_s}{GM_s}, \tag{5}$$

$$S = \frac{L_s V_0}{\eta}, \tag{6}$$

where plasma β is the ratio of the thermal to the magnetic pressures, c_s and c_A denote the sound and Alfvén speeds, respectively, V_0 is a typical speed of the system, L_s is a typical length scale in the system, G is the gravitational constant, M_s denotes the solar mass, and η is resistivity. We neglect explicit viscosity in the model presented here. For simplicity, we study the isothermal case ($\gamma = 1$) and therefore $p = nk_B T_0$. Here, n is particle density, k_B denotes Boltzmann's constant, and T_0 is plasma temperature. Such an assumption is justified as most of the *TRACE* loops were observed at a chosen temperature, generally at close to 1 MK (Fe IX 171 Å filter).

The normalizations of the variables in the MHD equations are $\mathbf{V}/v_A$, t/τ_A, $\mathbf{x}/L_s$, ϱ/ϱ_0, and B/B_0. We set the magnetic field strength of the dipole at $B_0 = 60$ G, temperature $T_0 = 1$ MK, and density $n_0 = \varrho_0/m_p = 10^9$ cm^{-3}, where m_p is the proton mass. These values correspond to the Alfvén speed $V_0 = 4138.57$ km s^{-1}, the isothermal sound speed $c_s = 128.5$ km s^{-1}, and Alfvén time $\tau_A = 16.8$ s. Resulting Euler and Froude numbers are given as $E_u = 9.64 \times 10^{-4}$ and $F_r = 9.03$. Furthermore, we introduce as a spatial unit $L_s = R_s/10 = 69.55$ Mm. We use the value of $S = 10^4$ in this study which means that the resistive diffusion time is 10,000 times smaller than the Alfvén transit time. Thus, we are in the low-resistivity regime. The smallest value of resistivity that can be represented in a numerical code is determined by the resolution of the grid. Although the resistivity in the model is likely still higher than in the solar corona, on the typical timescale of oscillations of order 100 Alfvén times considered in this study the resistivity does not affect the magnetic field significantly.

2.1. Numerical Code

We adopt the numerical code *NLRAT* described by Ofman & Thompson (2002) and developed by Ofman (2007). This code implements the modified Lax–Wendroff scheme with a fourth-order Chebyshev smoothing term added for stability (Hamming 1973, p. 571) for solving time-dependent non-ideal isothermal MHD equations. Powell's method is used for the correction of the divergence of the magnetic field.

Equations (1)–(3) are solved numerically in an Eulerian box with the x, y, and z dimensions $(x_{\min}, x_{\max}) \times (y_{\min}, y_{\max}) \times (z_{\min}, z_{\max}) = (-3.5, 3.5) \times (-3.5, 3.5) \times (1, 5.5)$ or $(x_{\min}, x_{\max}) \times (y_{\min}, y_{\max}) \times (z_{\min}, z_{\max}) = (-3.5, 3.5) \times (-3.5, 3.5) \times (3, 7.5)$. All spatial coordinates are given in units of L_s. The numerical box is covered by a uniform grid of $150 \times 150 \times 130$ numerical cells. Grid convergence studies showed that this resolution is sufficient to resolve the loop and get results independent of the grid.

We apply open boundary conditions, with a zero-gradient extrapolation of all plasma variables at all the boundaries except at $z_{\min}$, which corresponds to the photospheric boundary to allow a wave signal to leave freely the simulation region. At the bottom of the simulation region ($z_{\min}$), we model wave reflection from the photospheric layer ($z < z_{\min}$) by introducing line-tying boundary conditions:

$$\mathbf{B}(x, y, z_{\min}, t) = \mathbf{B}(x, y, z_{\min} + \Delta z, t), \qquad (7)$$

$$\mathbf{V}(x, y, z_{\min}, t) = 0, \qquad (8)$$

$$\varrho(x, y, z_{\min}, t) = \varrho(x, y, z_{\min} + \Delta z, t). \qquad (9)$$

2.2. Initial Conditions

As the initial equilibrium magnetic field of our AR, we take an idealized 3D potential dipole. Magnetic fieldlines are shown in Figure 1. Detailed formulae describing such a magnetic configuration can be found in Ofman & Thompson (2002). As the initial background density, we use a gravitationally stratified equilibrium density which is the solution of Equation (2) in the equilibrium state (see also Equation (13) below):

$$\varrho(x, y, z, t = 0) = \varrho_0 \exp \left\{ \frac{1}{H} \left[\frac{1}{(10 + z - z_{\min})} - \frac{1}{10} \right] \right\}. \qquad (10)$$

Here, H is the normalized scale height expressed as

$$H = \frac{1}{E_u F_r} = \frac{2 k_B T_0 L_s}{G M_s m_p}. \qquad (11)$$

For the set of parameters given above $H = 8.7 \times 10^{-3}$, which corresponds to a scale height of 60.5 Mm, and plasma β varies with height (from 0.0025 at the center of the bottom of the simulation region to 0.5 at the center of the top of the simulation region).

2.3. The Loop

We model a denser loop located between a chosen set of magnetic fieldlines. Note that such a loop has a modified Alfvén speed in comparison to the ambient corona. We use a new approach to calculate the initial state of a loop, whose boundary exactly follows a flux tube in a dipole field. For test purposes, a few cases were also computed for an extended McLaughlin & Ofman (2008) approach of a "cylindrical loop," i.e., a loop with a fixed cross section constructed along a chosen fieldline, which is the axis of the loop.

While in McLaughlin & Ofman (2008) the increased density inside the loop was achieved by imposing a discontinuous jump between ϱ_i and ϱ_e, we use a smooth density profile which is closer to observations (Aschwanden et al. 2003), starting in the $x = 0$ plane:

$$\varrho_i = \varrho_e d \exp \left[-\left(\frac{(y - y_0)^2 + (z - z_0)^2}{w} \right)^2 \right]. \qquad (12)$$

Here, subscripts i(e) refer to the loop (ambient corona) and d denotes the density ratio between the loop and ambient corona. A value of $d = 3$ is chosen, in agreement with observations of loops oscillating in the horizontal kink mode (Aschwanden et al. 2003) and in the vertical kink mode (Selwa et al. 2007). $(x_0, y_0, z_0) = (0, 0, 4)$ or $(x_0, y_0, z_0) = (0, 0, 5.25)$ denote the central point of the fieldline chosen as the loop's axis for different loops; $w = 0.375$ is the loop width at the apex.

We study two kinds of loop geometries: closed geometry and open geometry. The closed geometry loop is defined as a loop which has maximum separation between its legs at the middle of the loop's height, while the open geometry loop has a maximum separation between its legs at the footpoints. Note that this nomenclature does not reflect the amount of open flux in the simulation box. The closed geometry loop resembles the loop from the McLaughlin & Ofman (2008) studies, while the open geometry loop shows more resemblance to the arcade loop from the Selwa et al. (2005, 2006, 2007) studies. We obtain the open geometry loop by shifting the photosphere level along the vertical axis. The density profiles along the $y = 0$ cut together with 3D plots of the loop and fieldlines of these loops are shown in Figure 1 (gravitational stratification is neglected to enhance clarity in the figure; the computations are carried out with gravitational stratification included). The plotted loops correspond to the new approach, with variable cross section, such that the loop's boundary traces fieldlines. The loop width $w = 0.375$ is chosen for two reasons: (1) it is sufficiently wide to have several grid points in the footpoint of the loop (2) and is also sufficiently wide to resolve the boundary of the loop.

We calculate the initial state of the flux-tube-filling loop in a way that we start tracing the loop in the $x = 0$ plane. Each of the fieldlines is parameterized with a factor associated with the value of the Gaussian profile (Equation (12)) which is constant along the whole fieldline in the flux tube in case (2).

From the momentum Equation (2) in equilibrium it follows that for such an equilibrium configuration the sum of the Lorentz force, hydrostatic force, and gravitational force must vanish:

$$E_u \nabla p - (\nabla \times \mathbf{B}) \times \mathbf{B} + \frac{\varrho \hat{\mathbf{z}}}{F_r (R_s + z - z_{\min})^2} = 0. \qquad (13)$$

As the initial magnetic field is potential $(\nabla \times \mathbf{B}) = 0$ and plasma β (Euler number) is small in the system, the equilibrium density profile is the same inside and outside the loop and varies just by a factor of d. For the same reason, we can choose a density distribution that is not in exact force balance in the initial state (e.g., constant radius loop following a fieldline in a dipole field). Consequently, our loop is near the equilibrium state at $t = 0$. However, we expect small adjustments of the loop across fieldlines during the initial stage of the simulation. In the
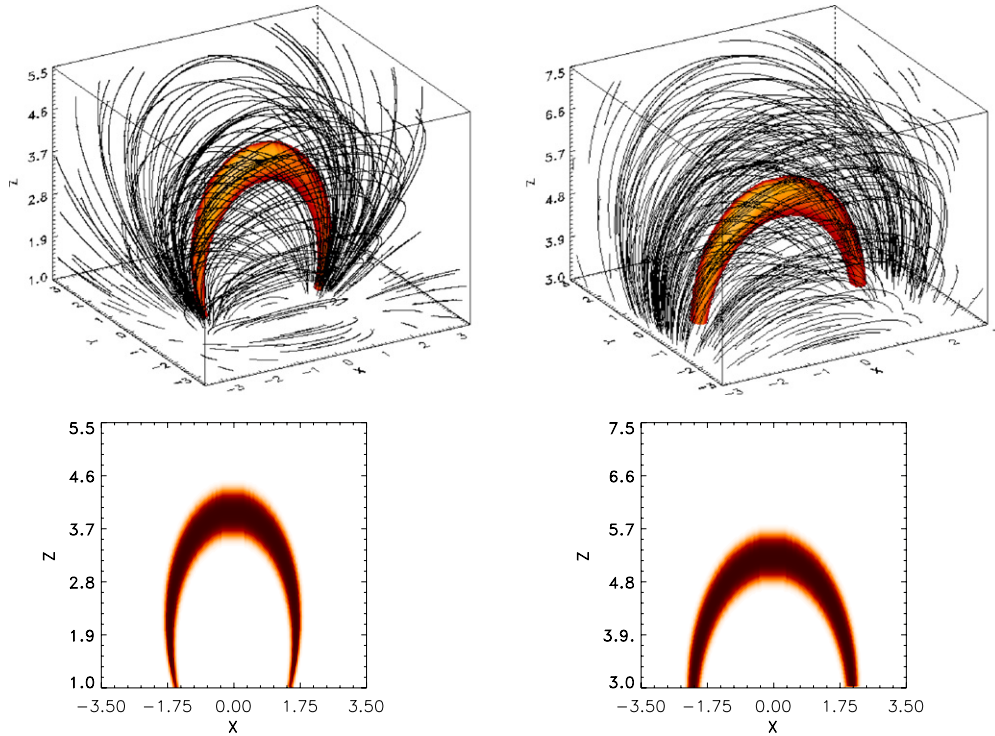
Figure 1. Initial 3D magnetic field configuration of the magnetic field with the flux tube loop for the closed geometry (left panels) and open geometry (right panels) loops. The top panels present the fieldlines together with the isosurface of density, while the bottom panels display the loop density cut along the $y = 0$ line. Note that gravitational stratification is neglected in both cases in order to display the loop more clearly (but the oscillations are computed in the presence of gravitational stratification). Spatial coordinates are measured in units of L_s. The vertical axis is stretched relative to the horizontal axis in the lower frames.

(A color version of this figure is available in the online journal.)

3D MHD model, the loop rapidly achieves an equilibrium state through the generation of a small magnetic pressure gradient at the loop boundary that balances the thermal pressure inside the loop.

2.4. The Perturbation

In order to excite kink oscillations, we perturb the loop in the following ways: by initial velocity perturbations (Gaussian blobs) and by a non-initial pulse originating from the z boundary (2D, time-dependent, boundary perturbation). The first type of perturbation is a 3D extension of the perturbation used by Selwa et al. (2005, 2006, 2007) in 2D arcade studies and consists of an initial ($t = 0$) 3D structure (which is not imposed as a boundary condition and is not time dependent) in V_z with a Gaussian shape, located below the loop, but above the boundary:

$$V_z = A_V V_{A0} \exp[-(4x^2 + 4y^2 + 2(z - z_0)^2)^2]. \qquad (14)$$

Here, $A_V = 0.1$ is the relative amplitude of the pulse, V_{A0} is the maximum Alfvén speed at the bottom of the simulation region, and $z_0 = 1(2)$ in the case of closed geometry or 3(4) in the case of open geometry loops, for two locations of the perturbation, respectively. Such a structure is either placed below the loop close to the photospheric boundary (top panels of Figure 2) or it is located higher up, centered within the loop (bottom panels of Figure 2).

Another type of perturbation considered here models an impulsive event (flare) centered below the loop legs (velocity

pulse launched at the bottom boundary, Figure 3):

$$V_z = A_V V_{A0} \exp\left[-\left(\frac{x - x_0}{w}\right)^2\right] \exp\left[-\left(\frac{y - y_0}{w}\right)^2\right]$$

$$\times \exp\left[-\left(\frac{2t - \left(t_1 + \frac{t_2 - t_1}{2}\right)}{t_2 - t_1}\right)^8\right], \qquad (15)$$

where $A_V = 0.1$ is the relative amplitude of the pulse, V_{A0} is the maximum Alfvén speed at the bottom of the simulation region $t_1 = 2.5\tau_A$, $t_2 = 7.5\tau_A$, $w = 1.0$, and $x_0 = 0$, $y_0 = 0$ (A).

3. NUMERICAL RESULTS

3.1. Geometry of the Loop

We start our studies with the loop shown in the left panels of Figure 1. Looking for vertical kink oscillations, we perturb the loop by the initial velocity perturbations shown in Figure 2 (Equation (14)) and by the pulse below the loop in the vertical component of velocity, V_z (bottom panel of Figure 3, Equation (15)).

The behavior of the 3D closed geometry loop perturbed from the bottom is plotted in the top panels of Figure 4. Only the upper part of the loop oscillates vertically. Similar oscillations of the upper half of the loop are excited when we change the boundary pulse to the initial perturbation at the photospheric level or in the middle of the loop so that it is located equally distant from all parts of the loop (not shown). The lower parts of the loop remain almost unperturbed. In order to relate our results to satellite observations, we generate 2D difference images of
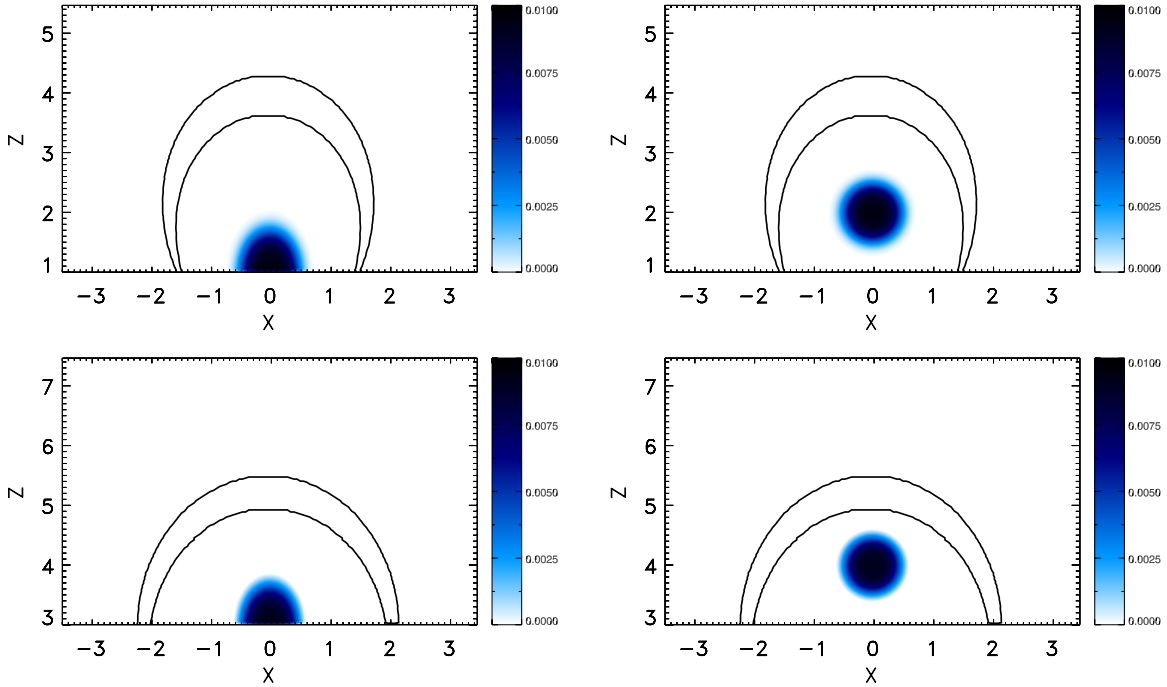
Figure 2. Spatial profiles of the perturbation in the x–z plane cutting through the axis of the loop ($y = 0$) given at $t = 0$ (color scales) launched at photospheric level (top panels) and above—fitting the shape of the loop (bottom panels) in the case of the closed (left panels) and open (right panels) geometry loops. Black contours show the profile of the loop. Spatial coordinates are given in units of L_s.
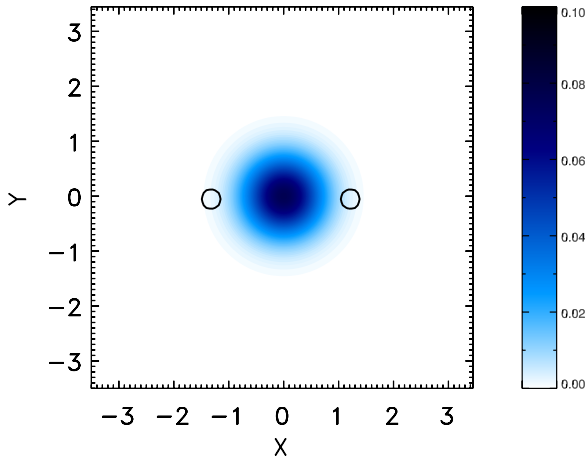
(A color version of this figure is available in the online journal.)

Figure 3. Spatial profiles of the pulses launched in the z component of velocity (bottom panel, x–y plane at $z = 1$; color scale). Black contours display the initial position of the loop (different plane than the pulse in the top panel). Spatial coordinates are given in units of L_s.

(A color version of this figure is available in the online journal.)

the oscillating loops (commonly used to enhance and visualize small-scale dynamics in observational data) by taking cuts in the plane through the loop in the 3D model and calculating running differences between the frames. The difference images in all these cases are quite distinct from the oscillation of the loop modeled in 2D arcade geometry by Selwa et al. (2005, 2006, 2007), corresponding to a "breathing-like" motion (i.e., loop changing position up and down; a similar signature was also found by Wang & Solanki 2004 using a simple geometrical model).

A possible explanation of this mechanism may be that the non-uniform width of the loop causes non-uniform oscillation within the loop. To examine the impact of this feature, we change

the geometry of the loop to the cylinder surrounding a chosen fieldline. Difference images for a cylindrical loop proved that the oscillation seems to be restricted to the upper part of the loop (just as in the case of the flux tube loop), while the lower parts of the loop remain unperturbed, as can also be seen in Figure 7 of McLaughlin & Ofman (2008).

The excitation of the oscillation based on whole loop displacement (as shown in 2D by Selwa et al. 2005, 2006, 2007) may be associated with the shape of the loop. The 3D open geometry loop is similar to the 2D potential arcade loop discussed by Selwa et al. (2005, 2006, 2007). Difference images of oscillations excited by the boundary pulse are shown in Figure 5. We clearly see that the loop is displaced as a whole, and the highest amplitude of the oscillation corresponds to the upper part of the loop (as suggested by Wang & Solanki 2004, irrespective of the perturbation type studied in this paper, not shown).

A possible explanation of the difference in the vertical oscillation affecting part of the loop or the whole structure is associated with the way the Lorentz ($\mathbf{j} \times \mathbf{B}$) force acts on the loops of closed and open geometries (Figure 6). As we are interested only in vertical oscillations, Figure 6 shows only x and z components of the Lorentz force. The Lorentz force dominates in a curved (and low β) structure in comparison to the thermal pressure gradient force, i.e., the total force acts on both the loops in the same way as the Lorentz force. The ratio of magnetic and thermal pressure is not the same in the two configurations studied here, even if they match at one or two points (e.g., apex and footpoints). The difference between the two geometries is striking: in the closed loop the Lorentz force at the footpoints is largest, and directed inward, opposing the oscillations, while in the open loop the Lorentz force is largest at the apex and supports oscillations as it moves the loop as a whole. In the closed geometry loop, the Lorentz force changes sign at a quarter of the loop length: while vertical oscillation results in an upward shift of the apex (the part which supports vertical oscillations),
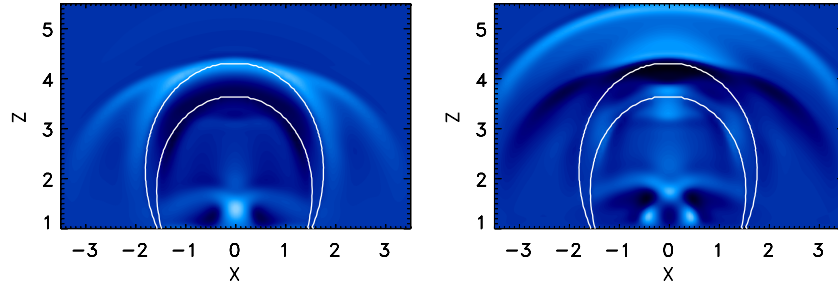
Figure 4. Running difference images in the *x*–*z* plane (at *y* = 0) of mass density of the closed geometry loop between the initial state and the first maximum in time signature (left panel) and between the first maximum and the first minimum (right panel), respectively. The perturbation is launched as a z_{min} boundary pulse (corresponding to the perturbation shown in Figure 3). White contours correspond to the initial position of the loop. Light (dark) blue areas correspond to an increase (decrease) in density. Spatial coordinates are given in units of L_s.

(A color version of this figure is available in the online journal.)
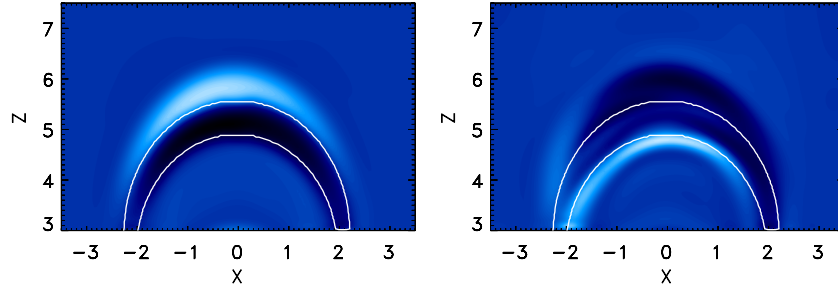
Figure 5. Same as Figure 4, but for the open geometry.

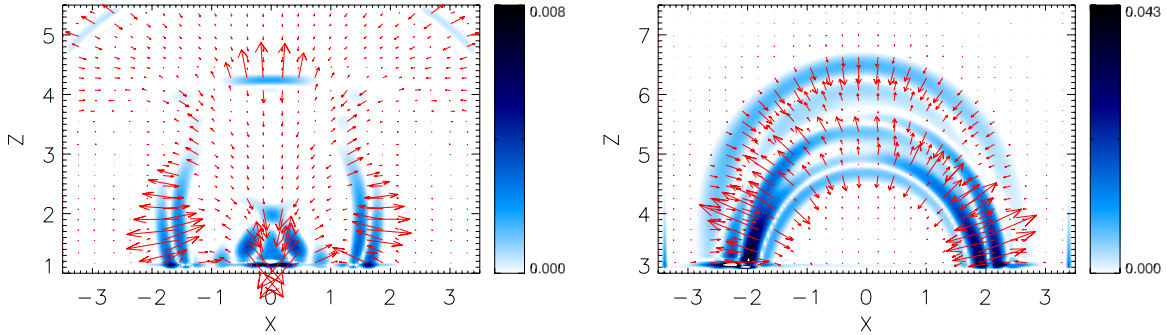(A color version of this figure is available in the online journal.)

Figure 6. Lorentz force ($|\mathbf{j} \times \mathbf{B}|$, only *x* and *z* components considered in this figure, the magnitude is plotted with color scale, while the arrows show the direction) acting on a loop of closed (left panel) and open (right panel) geometry just before the second maximum displacement of the loop along the *y* = 0 plane. The perturbation was launched as a z_{min} boundary pulse (corresponding to perturbation shown in Figure 3). Spatial coordinates are given in units of L_s; $|\mathbf{j} \times \mathbf{B}|$ (color scale) is given in arbitrary units; red arrows show the direction of $\mathbf{j} \times \mathbf{B}$.

(A color version of this figure is available in the online journal.)

the loop legs are squeezed together (contrary to the "breathing" motion described by Wang & Solanki 2004) and counteract the oscillation due to the change of sign of curvature (i.e., inflection point). The scenario for the open geometry loop is different: the curvature does not change the sign anywhere from its legs to the apex and leads to a coherent Lorentz force shifting the whole loop away from the disturbance. Note that the magnitude of the Lorentz force is the highest at the footpoints in both directions as the magnetic field is strongest at the bottom of the simulation region, plasma β reaches its minimum value, and moving the magnetic fieldlines needs a stronger force than the apex of the loop. As the plots from the simulations (Figure 6) are affected by the component of the force directed toward the center of the loop, we present corresponding schematic figures (Figure 7) for better explanation of the mechanism.

The geometry of the loop observed by Wang & Solanki (2004) is closed rather than open, so we expect the vertical

kink oscillation to be localized in the upper part of the loop rather than displacing the loop as a whole. To examine this feature, we reanalyze the event from 2002 April 17 observed by *TRACE* (195 Å). Panel (a) of Figure 8 shows two loops before the oscillation took place. The loop outlined with diamonds was found to oscillate in a vertical kink mode by Wang & Solanki (2004). Panels (b)–(d) of Figure 8 show difference images for maximum displacement of the loop. Colors are used to highlight the displacements more clearly than in the Wang & Solanki (2004) paper. We observe that mainly the upper part of the loop is displaced (with the possible exception of the lower footpoint in panel b), while there is almost no motion near the footpoints, which agrees well with the results of our simulation.

Next we estimate the period of oscillation:
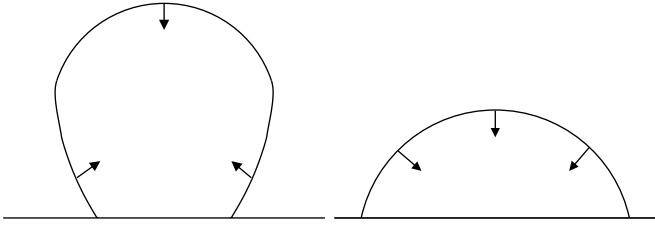
$$P = \frac{2L}{c_k}, \tag{16}$$

Figure 7. Schematic diagram showing maximum displacement of the loop of closed (left panel) and open (right panel) geometry during the oscillation (solid line contour). The arrows show the Lorentz force ($|\mathbf{j} \times \mathbf{B}|$ acting on the loop's apex and legs.

where P is the oscillation period of the fundamental kink mode, L is the length of the loop, and the kink speed c_k is calculated as

$$c_k = V_{Ai}\sqrt{\frac{2}{1 + \varrho_e/\varrho_i}}. \qquad (17)$$

Here, V_{Ai} is the Alfvén speed inside the loop and ϱ_e/ϱ_i is the density contrast between the outside and inside of the loop. Note that Equation (17) is strictly applicable only to the cylindrical straight loop with a discontinuous jump in density between

ϱ_i and ϱ_e and with otherwise constant density and magnetic field. In our loop, the density is not uniform along the loop due to gravity, the magnetic field is variable due to the dipole geometry, and the transition between ϱ_i and ϱ_e is continuous. Therefore, Equation (17) is only approximately applicable to the present loop model and to real coronal loops. We assume that the loop length is close to the length of the fieldline belonging to the midpoint of the apex (axis of the loop). We calculate the length using the finer grid used for fieldline tracing (initially five times finer than the grid used in 3D MHD calculations and refined according to the value of the magnetic field). For the given choice of central point of the loop, the loop length is $\sim 7L_s$, both for closed and open geometry loops. We assume a density contrast of $\varrho_e/\varrho_i = 1/d$, which is the difference between the loop's core and the surrounding plasma. The Alfvén speed inside the loop is approximated by a mean value between the footpoints and the apex and reaches $V_{Ai} = 0.45V_{A0}$ for a closed geometry loop and $V_{Ai} = 0.275V_{A0}$ for an open geometry loop. Therefore, theoretically predicted periods using Equation (16) for the closed, P_c, and open geometry, P_o, loops are $P_c = 24\tau_A$ and $P_o = 44\tau_A$, respectively. The periods that we observe in the simulations are $P_{cs} = \sim 12\tau_A$ for the closed geometry loop and $P_{os} = \sim 45\tau_A$ for the open geometry
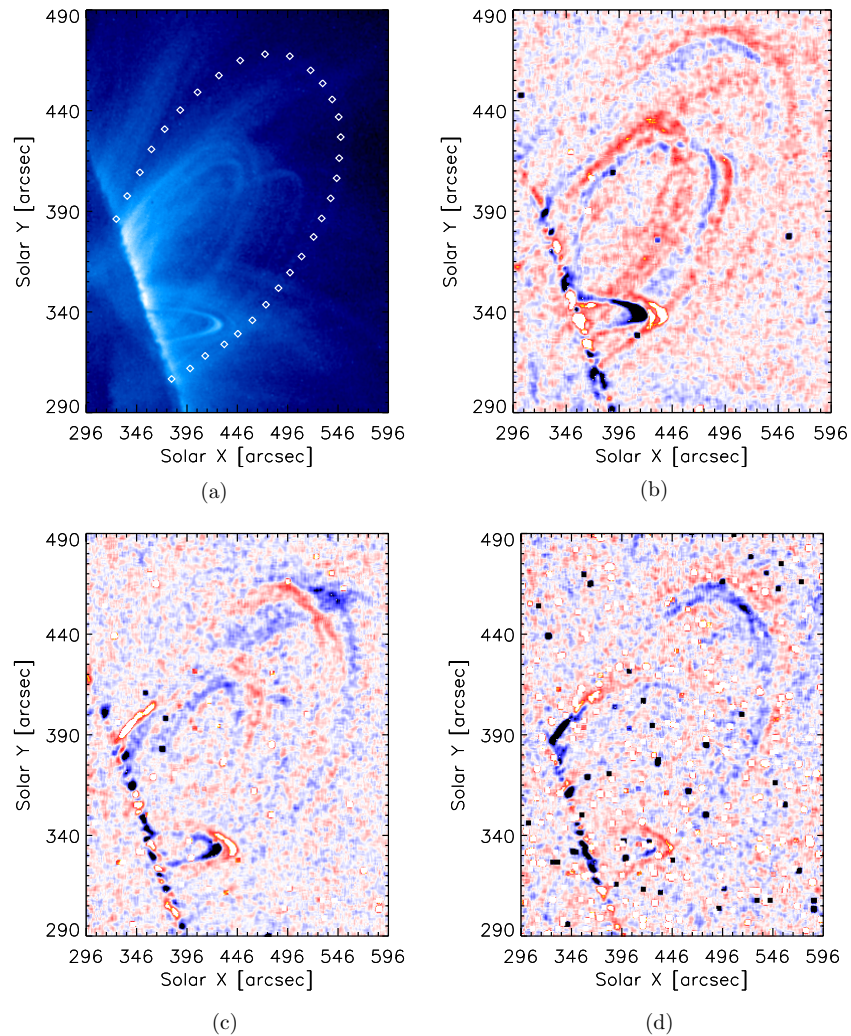

Figure 8. Observations of the oscillating *TRACE* loops in the 195 Å channel on 2002 April 17: image containing the analyzed coronal loop outlined by the diamonds at 11:22:07 (panel a), running difference images (11:24:57—panel b; 11:28:07—panel c; 11:29:49—panel d). Blue color indicates where the loop was in the earlier image and red where it has moved to (after Wang & Solanki 2004).

(A color version of this figure is available in the online journal.)

loop. Although the period obtained in simulations of the closed geometry loop is half the predicted value, the oscillation does not correspond to the second harmonic of the vertical kink mode (see difference images in Figure 4—there is no node at the apex as expected from the second harmonic). Such a reduction in the period may originate from the partial oscillation of the loop. A similar ($P_c/P_{cs} \approx 2$) reduction in periods compared to analytical values was observed also by J. McLaughlin & L. Ofman (2008, private communication), where also only the top part of the loop oscillates and by Pascoe et al. (2009, difference images not shown) in the case of horizontal oscillations. Note that the period of the oscillation coincides with the analytical period of the fundamental kink mode in the case of the open geometry loop where the whole loop is displaced. Also, in the 2D case studied by Selwa et al. (2005) the period from numerical simulations matched the analytical period of the fundamental kink mode in a straight cylinder. Recently, De Moortel & Pascoe (2009) studied the problem of the difference between the theoretical and simulated periods and its effect on coronal seismology. The authors claim that the combined effects of the loop curvature, density ratio, and aspect ratio may lead to a reduction in periods. However, their arcade loop is more similar to our open geometry loop. Computations of horizontal oscillations of loops corresponding to our closed geometry would be useful. For the open geometry loop, the period from numerical simulations matches the analytically calculated one, so that these effects probably do not play such an important role. Hence, the geometry of the loop is a hitherto unrecognized, important factor determining the oscillations period. We find that the oscillation period is consistent with theoretical expectations if for L the length of only the part of the loop that oscillates is counted.

According to Nakariakov & Ofman (2001), the relative uncertainty in the value of the magnetic field strength, δB, is given as

$$\delta B = \sqrt{(\delta L)^2 + (\delta P)^2 + (\delta\rho/2)^2}, \qquad (18)$$

where δL, δP, and $\delta\rho$ are relative uncertainties in the estimation of the loop length, period of kink oscillation, and coronal plasma density, respectively. The loop geometry is an important factor and should be taken into account when estimating the magnetic field strength through coronal seismology, since it can lead to errors of ~50% in predicted periods of oscillations and also in the magnetic field strength (supposing that the period of oscillation and plasma density is measured without errors, i.e., $\delta P = \delta\varrho \simeq 0$).

Assuming that transversal oscillations are sensitive to the geometry of the loop, we check in how many cases would coronal seismology not work correctly if loop geometry is not taken into account and equations of straight cylinder oscillations are used. Figure 9 shows the histogram of oscillating loops (taken from the Aschwanden et al. 2002 and Wang & Solanki 2004 papers) versus the loop geometry. The geometry is presented based on circular fits to the loops, where the ratio h_0/r expresses the height of a circle center measured in the loop plane to the radius of the circular loop. A value of zero implies an exactly semicircular loop, positive values imply loops similar to our closed geometry, and negative values imply loops similar to our open geometry. We find that only 45% of all loops displaying transverse oscillations has $h_0/r \leqslant 0.1$, i.e., an open geometry. These loops can be used directly to estimate the coronal magnetic field. For the remaining 55% of the loops, the magnetic field is likely significantly overestimated. Note that
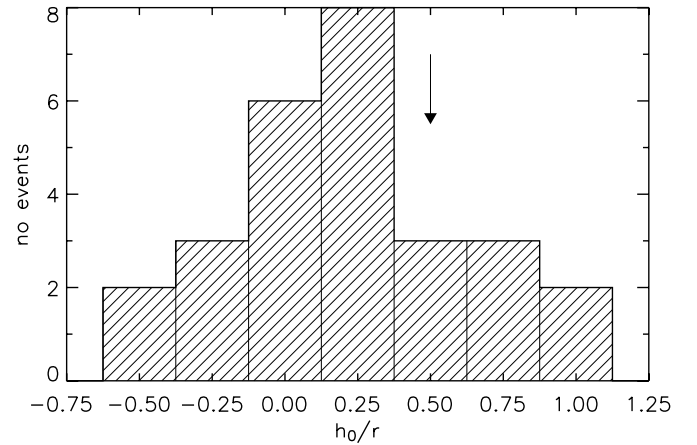

Figure 9. Histogram of kink oscillations analyzed by Aschwanden et al. (2002) and Wang & Solanki (2004). The number of oscillating loops is shown vs. the ratio of the height of the center of the best-fit circle measured in the loop plane, h_0, to the radius of the circular loop, r, expressing the geometry of the loop, based on data from Aschwanden et al. (2002) and Wang & Solanki (2004). The arrow indicates the h_0/r value obtained for the closed loop studied in this paper (left panel of Figure 1).

observed loops often have similar, or even larger, h_0/r values than the closed loop studied here, whose h_0/r is indicated by the arrow in Figure 9.

3.2. Damping of Kink Oscillations in AR Loop

As a possible damping mechanism, we find that the leakage of wave energy from the loop is the main process (Smith et al. 1997). It was found by Selwa et al. (2005, 2007) that vertical oscillations in the 2D arcade loop are damped through energy leakage. This was confirmed by McLaughlin & Ofman (2008) in 3D geometry. Selwa et al. (2005, 2007) detected short period (compared to global kink mode period) waves propagating out of the loop in the direction of decreasing Alfvén speed (above the loop) in the sausage mode. In 3D geometry, the scenario may be more complicated. Figure 10 shows the time signatures of the perturbed mass density (top panel), z (vertical, middle panel), and y (horizontal, top panel) components of velocity inside the loop and in its nearby surroundings along the horizontal line at $x = 0$, $z = 5.25$ (at the loop's apex and its surroundings) after excitation with the pulse centrally located below the loop (bottom panel of Figure 3, Equation (15)). We observe pure vertical kink mode oscillations of the loop (middle panel of Figure 10) and corresponding sausage mode oscillations (with maximum amplitude just after impact of the pulse exciting the kink mode) in the horizontal direction (bottom panel Figure 10). As the sausage mode is leaky, it will leak energy trapped in the loop due to the vertical kink oscillation in the form of a horizontal sausage wave.

Brady et al. (2006) and Verwichte et al. (2006) modeled 2D arcades and searched for leaky and body modes. They found that damping of oscillations depends on Alfvén speed profiles across the loop and surrounding plasma. The constant Alfvén speed atmosphere (with a dip at the loop) results in a lower leakage rate and slower damping (this is the usual case for a straight cylindrical loop) than for a non-constant Alfvén speed profile. Here we consider a similar scenario in 3D. From Figure 11, we see that the barrier in Alfvén speed for wave tunneling is lowest in the vertical (z) direction. However, time signatures show that the oscillation is damped mainly in the horizontal (y) direction. But during the vertical kink oscillation the loop
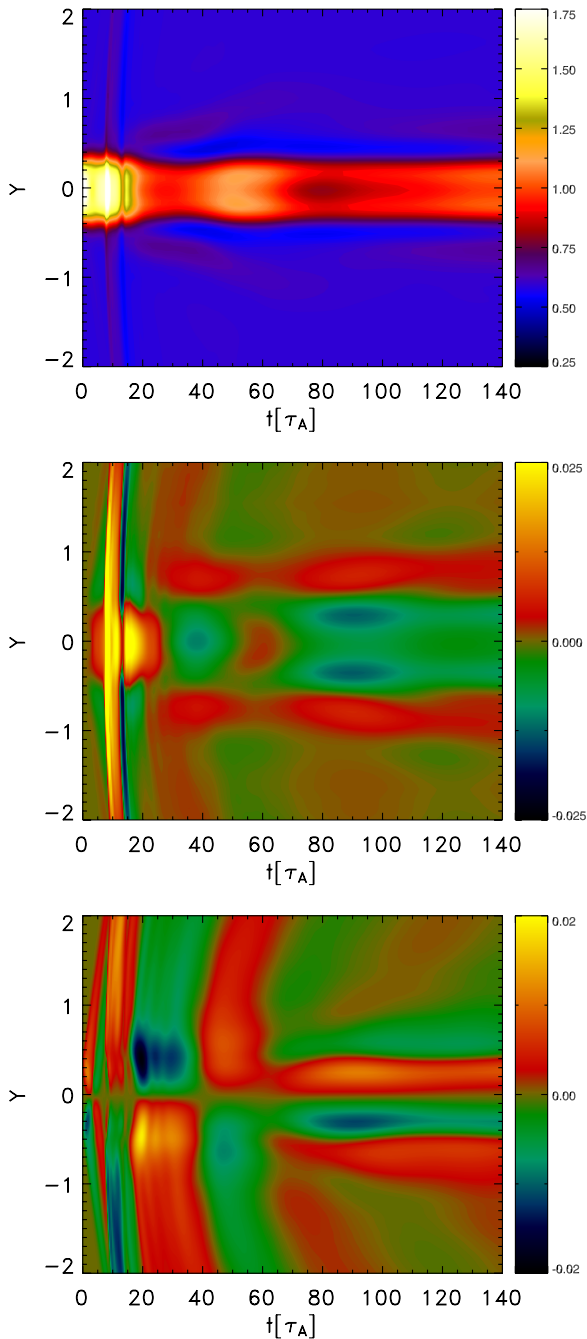
Figure 11. Alfvén speed profiles of the open geometry loop and surroundings (in units of V_{A0}) through the apex of the loop in all directions. Spatial coordinates are given in units of L_s.

Figure 10. Time signatures (color contours, units of ϱ_0 and V_{A0}, respectively) of mass density (top panel), vertical (V_z, middle panel), and transversal (V_y, bottom panel) component of velocity collected at the apex of the open geometry loop and its surroundings (along $x = 0$, $z = 5.25$ line). The loop was perturbed by a bottom boundary pulse corresponding to that shown in Figure 3. Spatial coordinates are given in units of L_s.

(A color version of this figure is available in the online journal.)

moves downward and upward (toward $z_{\min}$ or $z_{\max}$ boundaries). When the apex of the loop is shifted downward we end up with an Afvén speed profile that prevents tunneling (the barrier is higher). When the apex is shifted upward we might end up in a regime where no tunneling is necessary for the wave to leak or just with a mode that is more leaky than the original one. Leakage depends on the amplitude of oscillations: the higher the amplitude of the oscillation is, the more the leakage is enhanced and the damping time gets shorter. This agrees with the results
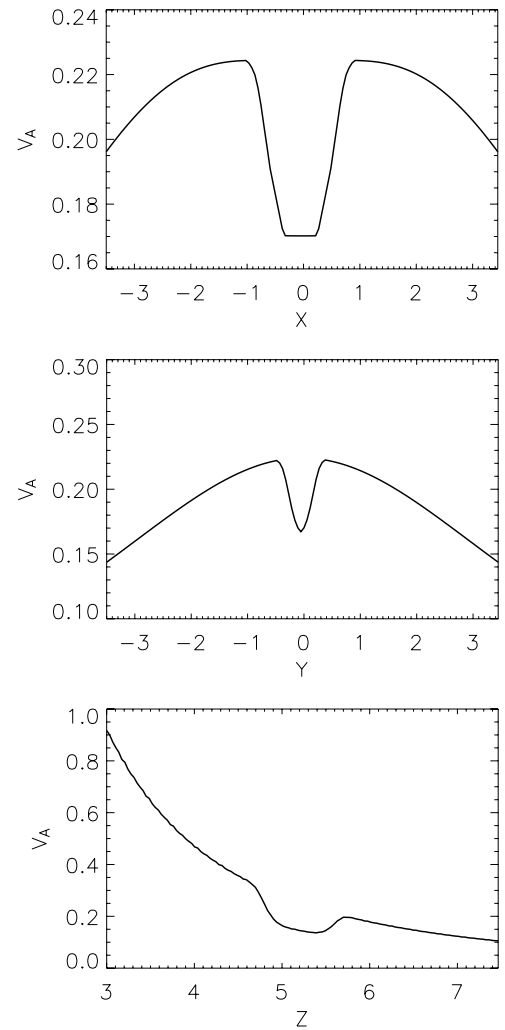
of Selwa et al. (2006), who showed that damping time decreases with the amplitude of the pulse as well as with the shift of the apex of the loop. The same mechanism would also work for a purely horizontal mode as the height of the apex changes during the oscillation.

4. SUMMARY AND CONCLUSIONS

We studied impulsive excitation of 3D oscillations of dense, gravitationally stratified loops using a 3D MHD model of an idealized AR dipolar magnetic field. We varied the geometrical properties of the loops and the pulse and investigated their impact on the modes of oscillations. We find that loops with maximum separation at the footpoints (open geometry loops) exhibit global vertical mode oscillations. This confirms the results of previous 2D MHD studies of arcade loops by Selwa et al. (2005, 2006, 2007). However, for loops having maximum separation in the middle, i.e., closed geometry loops that expand with height beyond their photospheric footpoints, only their upper part shows oscillations in a vertical kink mode. The periods of such oscillations are shorter than the analytically predicted ones, due to the reduced effective length of the loop that takes part in the oscillations. We find that the value of the phase speed is not constant along the loop due to the

variation of both the magnetic field and loop density with height and the applicability of the analytically derived kink speed c_k; Equation (17) is only approximate in the present, more realistic case. Such a reduction was also observed in a curved cylindrical loop in a dipolar AR (McLaughlin & Ofman 2008) and in a 3D arcade loop in the case of horizontal oscillations (Pascoe et al. 2009; De Moortel & Pascoe 2009). Therefore, the difference between the loop length and the oscillating part of the loop should be considered while evaluating magnetic field strength through coronal seismology as it can lead to $\sim$50% errors in predicted oscillation periods and magnetic field strength.

We studied the damping of the oscillations in the curved AR loops and found that vertical kink waves in 3D stratified geometry are damped mainly due to wave leakage in the horizontal direction. We found that due to the rapid leakage, there was no time for the resonant absorption layers to form, and other dissipation mechanisms did not play an important role in the damping of vertical kink mode oscillations. We investigated the statistics of coronal loop geometries (open and closed) observed by *TRACE* (Aschwanden et al. 2002), compared our numerical results in detail to *TRACE* EUV observations of vertical loop oscillation with closed geometry seen on 2002 April 17 (Wang & Solanki 2004), and found good agreement with the observed damped vertical oscillation.

REFERENCES

Aschwanden, M. J., De Pontieu, B., Schrijver, C. J., & Title, A. M. 2002, Sol. Phys., 206, 99
Aschwanden, M. J., Fletcher, L., Schrijver, C., & Alexander, D. 1999, ApJ, 520, 880
Aschwanden, M. J., Nakariakov, V., & Melnikov, V. 2004, ApJ, 600, 458
Aschwanden, M. J., Nightingale, R. W., Andries, J., Goossens, M., & Van Doorsselaere, T. 2003, ApJ, 598, 1375
Berghmans, D., & Clette, F. 1999, Sol. Phys., 186, 207
Brady, C. S., Verwichte, E., & Arber, T. D. 2006, A&A, 449, 389
De Moortel, I., Ireland, J., Walsh, R. W., & Hood, A. W. 2002, Sol. Phys., 209, 61
De Moortel, I., & Pascoe, D. J. 2009, ApJ, 699, L72
Gruszecki, M., Nakariakov, V. M., van Doorsselaere, T., & Arber, T. D. 2010, Phys. Rev. Lett., 105, 055004
Hamming, R. W. 1973, Numerical Methods for Scientists and Engineers (2nd ed.; New York: McGraw-Hill)
Kliem, B., Dammasch, I. E., Curdt, W., & Wilhelm, K. 2002, ApJ, 568, L61
McLaughlin, J., & Ofman, L. 2008, ApJ, 682, 1338
Nakariakov, V. M., Aschwanden, M. J., & van Doorsselaere, T. 2009, A&A, 502, 661
Nakariakov, V. M., Melnikov, V. F., & Reznikova, V. E. 2003, A&A, 412, 7
Nakariakov, V. M., & Ofman, L. 2001, A&A, 372, L53
Nakariakov, V. M., Ofman, L., Deluca, E. E., Roberts, B., & Davila, J. M. 1999, Science, 285, 862
Nakariakov, V. M., & Verwichte, E. 2005, Liv. Rev. Sol. Phys., 2, 3
Ofman, L. 2005, Adv. Space Res., 36, 1572
Ofman, L. 2007, ApJ, 655, 1134
Ofman, L. 2009a, ApJ, 640, 502
Ofman, L. 2009b, Space Sci. Rev., 149, 153
Ofman, L., & Aschwanden, M. J. 2002, ApJ, 576, L153
Ofman, L., & Thompson, B. 2002, ApJ, 574, 440
Ofman, L., & Wang, T. J. 2002, ApJ, 580, L85
Pascoe, D. J., De Moortel, I., & McLaughlin, J. A. 2009, A&A, 505, 319
Robbrecht, E., Berghmans, D., & Poedts, S. 1999, in Plasma Dynamics and Diagnostics in the Solar Transition Region and Corona, ed. J.-C. Vial & B. Kaldeich-Schümann (ESA SP-446; Noordwijk: ESA), 575
Roberts, B., Edwin, P. M., & Benz, A. O. 1984, ApJ, 279, 857
Ruderman, M. S., & Erdélyi, R. 2009, Space Sci. Rev., 149, 199
Ruderman, M. S., & Roberts, B. 2002, ApJ, 577, 475
Schrijver, C. J., Aschwanden, M. J., & Title, A. M. 2002, Sol. Phys., 206, 69
Selwa, M., Murawski, K., & Kowal, G. 2004, A&A, 422, 1067
Selwa, M., Murawski, K., Solanki, S. K., & Wang, T. J. 2007, A&A, 462, 1127
Selwa, M., Murawski, K., Solanki, S. K., Wang, T. J., & Shumlak, U. 2006, A&A, 454, 653
Selwa, M., Murawski, K., Solanki, S. K., Wang, T. J., & Tóth, G. 2005, A&A, 440, 385
Selwa, M., & Ofman, L. 2009, Ann. Geophys., 27, 3899
Selwa, M., & Ofman, L. 2010, ApJ, 714, 170
Smith, J. M., Roberts, B., & Oliver, R. 1997, A&A, 317, 752
Terradas, J., & Ofman, L. 2004, ApJ, 610, 523
van Doorsselaere, T., Verwichte, E., & Terradas, J. 2009, Space Sci. Rev., 149, 299
Verwichte, E., Foullon, C., & Nakariakov, V. 2006, A&A, 449, 769
Verwichte, E., Nakariakov, V. M., Ofman, L., & Deluca, E. E. 2004, Sol. Phys., 223, 77
Wang, T. J., & Solanki, S. K. 2004, A&A, 421, L33
Wang, T. J., Solanki, S. K., Curdt, W., Innes, D. E., & Dammash, I. E. 2002, ApJ, 574, L101
Wang, T. J., Solanki, S. K., Innes, D. E., Curdt, W., & Marsch, E. 2003, A&A, 402, L17